Performance Leap of Lithium Metal Batteries in $LiPF_6$ Carbonate Electrolyte by a Phosphorus Pentoxide Acid Scavenger

Jian Zhang,[1,#] Jiayan Shi,[2,3,#] Leo W. Gordon,[4] Nastaran Shojarazavi,[2] Xiaoyu Wen,[2] Yifan Zhao,[1] Jianjun Chen,[2] Chi-Cheung Su,[3] Robert J. Messinger,[4,] Juchen Guo[1,2,*]*

[1]Materials Science and Engineering Program, University of California – Riverside, Riverside, CA 92521, USA

[2]Department of Chemical and Environmental Engineering, University of California – Riverside, Riverside, CA 92521, USA

[3]Chemical Sciences and Engineering Division, Argonne National Laboratory, Lemont, IL 60439, USA

[4]Department of Chemical Engineering, The City College of New York, CUNY, New York, NY 10031, United States

AUTHOR INFORMATION

Corresponding Author

*E-mail: rmessinger@ccny.cuny.edu; jguo@engr.ucr.edu

Keywords: Phosphorus pentoxide, Lithium metal battery, Liquid electrolyte, Solid electrolyte interphase, Acid scavenger

ABSTRACT

Phosphorus pentoxide (P_2O_5) is investigated as an acid scavenger to remove the acidic impurities in a commercial lithium hexafluorophosphate ($LiPF_6$) carbonate electrolyte to improve the electrochemical properties of Li metal batteries. Nuclear magnetic resonance (NMR) measurements reveal the detailed reaction mechanisms of P_2O_5 with the $LiPF_6$ electrolyte and its impurities, which removes hydrogen fluoride (HF) and difluorophosphoric acid (HPO_2F_2) and produces phosphorous oxyfluoride (POF_3), $OF_2P\text{-}O\text{-}PF_5^-$ anions, and ethyl difluorophosphate ($C_2H_5OPOF_2$) as new electrolyte species. The P_2O_5-modified $LiPF_6$ electrolyte is chemically compatible with a Li metal anode and $LiNi_{0.6}Mn_{0.2}Co_{0.2}O_2$ (NMC622) cathode, generating a PO_xF_y-rich solid electrolyte interphase (SEI) that leads to highly reversible Li electrodeposition, while eliminating transition metal dissolution and cathode particle cracking. The excellent electrochemical properties of the P_2O_5-modified $LiPF_6$ electrolytes are demonstrated on Li||NMC622 pouch cells with 0.4 Ah capacity, 50-μm Li anode, 3 mAh cm^{-2} NMC622 cathode, and 3 g Ah^{-1} electrolyte/capacity ratio. The pouch cells can be galvanostatically cycled at C/3 for 230 cycles with 87.7% retention.

Introduction

High-energy-density lithium-ion batteries are arguably the most critical component in society's quest to electrify transportation. Li metal anodes hold the greatest promise for significantly increasing their energy density. However, Li metal anodes present fundamental challenges that have hindered commercialization such as dendrite formation and low cycling stability. One strategy to mitigate these challenges are to pair

them with solid- or semi-solid-state electrolytes, but low conductivities, various interfacial stabilities, high impedances, and difficulty in scale-up have been steep challenges for solid-state electrolytes.[1-3] On the other hand, liquid electrolytes have the advantages of high conductivity, facile charge transfer, and ease of integration into large-scale battery assembly and manufacturing lines. To date, the majority of liquid electrolytes demonstrating good performance in Li metal batteries are composed of fluorinated solvents and high concentrations of lithium salts containing weakly coordinating imide anions, including lithium bis(fluorosulfonyl)imide (LiFSI) and its derivates due to their high degree of dissociation.[4-10] A potential challenge for these electrolytes is the large costs of fluorinated solvents and high salt concentrations. In addition, many of the fluorinated solvents are not readily available and their long-term environmental and health impact are not clear.[11-15] LiFSI-based electrolytes may also corrode aluminum (Al) current collectors.[16,17] Therefore, it would be tremendously beneficial if Li metal batteries could be built using commercial Li-ion electrolytes containing lithium hexafluorophosphate ($LiPF_6$) and organic carbonate solvents, as commonly used in today's Li-ion batteries.

However, researchers have long known that $LiPF_6$ electrolytes are not compatible with Li metal anodes due to autocatalytic side reactions originating from trace amount of water in the electrolyte: a series of hydrolysis reactions starting from phosphorus pentafluoride (PF_5), which is formed during disproportionation of $LiPF_6$ into LiF and PF_5, generates hydrogen fluoride (HF).[18-21] HF passivates the Li anode surface, resulting in high overpotential and non-uniform deposition structure.[22] More

importantly, HF reacts with the SEI on the lithium metal to produce water, thus triggering the hydrolysis of PF_5 to form more HF and re-initiating the cycle. [23,24] Furthermore, HF also reacts with the transition metal cathode materials, causing the dissolution of transition metals [25,26] and cathode particle cracking. [27]

We hypothesize that the key detrimental property of commercial $LiPF_6$ electrolytes that prohibit their use in Li metal batteries is the presence of HF; therefore, a reagent that can scavenge HF and break the deleterious autocatalytic cycle should vastly improve electrochemical performance. Although HF scavenger materials has been previously studied, [28-30] there is no existing work that demonstrates superior cell performance in realistic Li metal pouch cells coupled with a detailed molecular-level study. Here, we validate this hypothesis by using phosphorus pentoxide (P_2O_5), a widely available acid scavenger with a strong hygroscopic nature,[31] to modify a commercial 1 M $LiPF_6$ electrolyte in mixed ethylene carbonate/diethyl carbonate solvent (EC/DEC, 50/50 volume ratio). The modification is simple: 5 wt.% of P_2O_5 was stirred in the commercial electrolyte for 24 hours at room temperature, followed by centrifugation and filtration to remove the remaining solid content. During this process the P_2O_5 scavenges water and HF, while reacting with electrolyte species to form soluble phosphorous-containing compounds that stabilize the lithium metal SEI, as shown below. Note that residual P_2O_5 is removed during the centrifugation step. Li||$LiNi_{0.6}Mn_{0.2}Co_{0.2}O_2$ (NMC622) pouch cells with 0.4 Ah capacity were then assembled and tested to compare the performance between the commercial and P_2O_5-modifed electrolytes. The pouch cells used a Li anode coated on both sides of a copper

current collector (50-μm on each side), a NMC622 cathode coated on both sides of an Al current collector (areal capacity of 3 mAh cm^{-2} on each side), and a lean electrolyte/capacity ratio of 3 g Ah^{-1} (1.2 g electrolyte per cell). All cells were cycled at C/10 in the first three cycles (activation) and subsequently charged at C/10 and discharged at C/3 in the following cycles.

Experimental Methods

Materials: The commercial electrolyte of 1 M $LiPF_6$ in a mixture of EC/DEC (50/50 volume ratio), battery grade, was purchased from Sigma-Aldrich. P_2O_5 (≥99.99%, trace metal basis, Sigma-Aldrich) was dried under vacuum at 80°C inside an argon-filled glovebox for 24 hours prior to use. The $LiNi_{0.6}Mn_{0.2}Co_{0.2}O_2$ (NMC622) cathode powder was purchased from Targray Technology International, Inc.

Electrodes preparation: The lab-made thin Li foil (50 μm in thickness) was prepared using a previously reported method.[22] The double-sided Li metal anode was prepared by sandwiching a copper foil (9 μm, MTI Corporation) with two pieces of lab-made Li metal foil and pressed with a mechanical roller. The cathode slurry was prepared by mixing 90 wt.% NMC622, 5 wt.% carbon black (Supper C65), and 5 wt.% polyvinylidene fluoride (PVDF, Sigma-Aldrich, M_w~534,000) in N-methyl-2-pyrrolidone (NMP, anhydrous, 99.5%, Sigma-Aldrich) with a centrifugal mixer (Thinky, AR-100) for 15 min. All the materials in the slurry preparation, except NMP, were dried under vacuum at 70 °C for 24 hours prior to use. NMP was dried with 3 Å molecular sieves prior to use. The mass ratio of liquid to solid in the slurry was 1.65. The slurry was coated with an automatic tape casting coater (MTI corporation) on to an aluminum

current collector (16 μm, Gelon LIB Group) with the film applicator set to 300 μm, which made a 3 mAh cm^{-2} NMC622 cathode sheet. The coated electrodes were transferred into the glovebox and dried at room temperature for 12 hours. Then, the electrodes were dried under vacuum inside glovebox at 120 °C for 12 hours prior to use. The thickness of electrodes (90 μm for single side) was controlled by calendaring with a mechanic roller. Single-sided and double-sided cathodes were prepared for coin cells and pouch cells, respectively.

Cell assembly and electrochemical experiments: Pouch cells were assembled inside an argon-filled glovebox. Celgard-2400 was used as the separator. The amount of electrolyte in the pouch cells was kept at 3 g Ah^{-1}. A lab-made pouch cell holder was used during cycling. The cycling experiments were performed with Neware battery testers under initial pressure loading of 10 psi using force sensitive resistor calibrated by Arduino microcontroller as shown in **Figure S1** in the supporting Information. A constant-current-constant-voltage charging protocol was used for all the Li||NMC622 cells: they were galvanostatically charged to 4.3 V and then held at 4.3 V until the current dropped to less than C/30 (1 C is defined as 1 mA cm^{-2}). For discharge, all cells were galvanostatically discharged to 2.5 V. The C rate for formation cycles (the first three cycles) was kept at C/20 for charging and discharging. After formation cycles, C/10 was used for charging and C/3 was used for discharging.

EIS analysis: EIS analysis was performed after the 10^{th}, 20^{th}, and 30^{th} cycles of the Li||NMC622 full cells. For the EIS measurement at each specific cycle, two identical cells were cycled at the same conditions. After cycling, these two cells were

disassembled and the same electrodes were reassembled to make Li||Li and NMC622||NMC622 symmetric cells with fresh separator and replenished electrolyte.[32,33] The EIS measurements were conducted using a Gamry potentiostat Interface 1000, scanning over the frequency range from 10^6 Hz to 0.01 Hz with a 2 mV amplitude.

Average coulombic efficiency measurement: CR-2016 type coin cells were used to measure the average coulombic efficiency (CE) of Li deposition and stripping: a lab-made Li foil with the thickness around 50 μm was first weighed and then pressed to a Cu substrate as the working electrode. An identical Li electrode was used as the counter electrode without weighing. Galvanostatic stripping was first applied to the working electrode under certain current for a certain period of time, followed by deposition with the same current and same period of time to complete one cycle. After a set number of cycles, any remaining Li on the working electrode was completely stripped using a 0.5 mA cm^{-2} current until the stripping cutoff potential (1 V) was reached. The average CE is calculated from the following equation:[34]

$$CE_{Average} = \frac{(T_s \times J + n \times C_C) \times A}{m_{Li} \times Q + n \times C_C \times A}$$

where n is the cycle number; Cc is the cycling capacity; T_s is the time to completely strip the working electrode; J is the current to complete stripping (0.5 mA cm^{-2}), A is the area of the working electrode (1.266 cm^{-2}), and m_{Li} is the initial mass of the Li working electrode. Q is the theoretical capacity of Li (3.86 mAh mg^{-1}). The CE is the average of seven individual measurements.

SEM, EDS, and FIB characterizations: The surface morphology and the thickness of the Li deposition were characterized using a scanning electron microscope (SEM, Nova Nano S450, 10 kV). The samples were retrieved from the cells in an argon-filled glovebox and washed with dimethyl carbonate thoroughly to remove any residual electrolyte. Prior to the SEM characterization, the samples were dried at room temperature for 24 hours inside the argon-filled glovebox. The samples were then transported to the SEM facility inside a stainless-steel tube with KF-flange sealing. The samples were loaded in the SEM using a glove-bag with argon purging gas without exposing to ambient environment. The elemental mapping of the samples was collected using an Energy Dispersive X-ray (EDX) spectrometer coupled with the SEM. A focused ion beam (Quanta^{TM} 3D 200i with Ga liquid metal ion source) was used to precisely prepare the cross-sectional image of the NMC622 cathode particles. The ion gun voltage was set to 30 kV, and the current was 30 nA and 7 nA for bulk milling and polishing, respectively.

XPS: X-ray photoelectron spectroscopy (XPS) spectra were collected using Kratos AXIS Supra (Al Kα=1486.7 eV) at UC Irvine Materials Research Institute (IMRI). The samples were prepared following the same procedure for SEM samples. The samples were transported to the XPS facility inside a stainless-steel tube with KF flange sealing filled with argon. Finally, the samples were loaded in the sample chamber in the glovebox integrated with Kratos AXIS Supra for XPS analysis. All peaks of XPS data were analyzed by Casa XPS and calibrated with the reference peak of C 1s at 284.6 eV (the adventitious carbon).[35] The relative atomic ratio was calculated using the following

equation:

$$RA_i = \frac{A_i/S_i}{\sum A_i/S_i} \times 100\%$$

RA_i: relative atomic ratio of component i

A_i: Area of the deconvoluted peak of component i

S_i: relative sensitivity factor for component i

The relative sensitivity factors for Kratos AXIS are:

C 1s	O 1s	F 1s	S 2p	N 1s	Li 1s
0.278	0.736	1	0.723	0.477	0.025

NMR spectroscopy: Liquid-state ^{1}H, ^{31}P, and ^{13}C NMR experiments were performed on a Bruker Avance III HD 600 NMR spectrometer with a 14.1 T superconducting magnet equipped with a Bruker 5-mm Triple Resonance Inverse Probe TXI (600S3 H-P/C-D-05 Z-gradient) operating at 600.13, 242.94, and 150.90 MHz for ^{1}H, ^{31}P, and ^{13}C nuclei, respectively. Liquid-state ^{19}F NMR experiments were performed on a Bruker Avance III HD 700 NMR spectrometer with a 16.4 T super-conducting magnet equipped with a 5 mm QCI-F cryoprobe (CP QCI 700S4 H/F-C/N-D-05 Z-gradient), operating at 658.78 MHz for ^{19}F nuclei. All liquid-state 1D single-pulse NMR spectra were acquired under quantitative conditions using 26, 21, 10, and 18 kHz rf field strengths for ^{1}H, ^{19}F, ^{31}P, and ^{13}C nuclei, respectively, as well as recycle delays of 12, 10, 25, and 30 s, after which all spins relaxed to thermal equilibrium. Liquid-state 2D $^{19}F\{^{31}P\}$ heteronuclear multiple-quantum correlation (HMQC) NMR experiments were performed on a Bruker Avance III 700 NMR spectrometer with a 16.4 T super-

conducting magnet equipped with a PAQXI probe ($^{1}H/^{19}F$, ^{31}P, ^{13}C, ^{15}N Z-gradient), operating at 658.78 MHz and 283.42 MHz for ^{19}F and ^{31}P nuclei, respectively, using 10 and 6 kHz rf field strengths.

DEMS: Differential electrochemical mass spectrometry (DEMS) experiment setup was reported in a previous study.[36] A commercially available GC-MS instrument (Shimadzu GCMS-QP2020 NX) was used. A glass capillary tube (Polymicro 1068150019) without any stationary phase on the inner wall was first sealed in the pouch cell using hot melt adhesive, and then the other end of the capillary tube was connected to the MS. The ion signals were quantified using standard gases.

Results and Discussion

As displayed in **Figure 1a**, the P_2O_5-modified $LiPF_6$ electrolyte strikingly improves the cycling stability of the Li||NMC622 pouch cells from less than 30 cycles to more than 200 cycles with an 87.7% capacity retention after 230 cycles. The pouch cell with the commercial $LiPF_6$ electrolyte experiences rapidly increasing charge-discharge hysteresis during cycling (**Figure 1b**), while the voltage profiles in the cells using the P_2O_5-modified electrolyte remain virtually unchanged throughout the same number of cycles (**Figure 1c**). The differential capacity profiles (dQ/dV) versus voltage (**Figure S2** in the Supporting Information) support the observation that the charge-discharge hysteresis of the cell with the P_2O_5-modified electrolyte does not change during cycling.

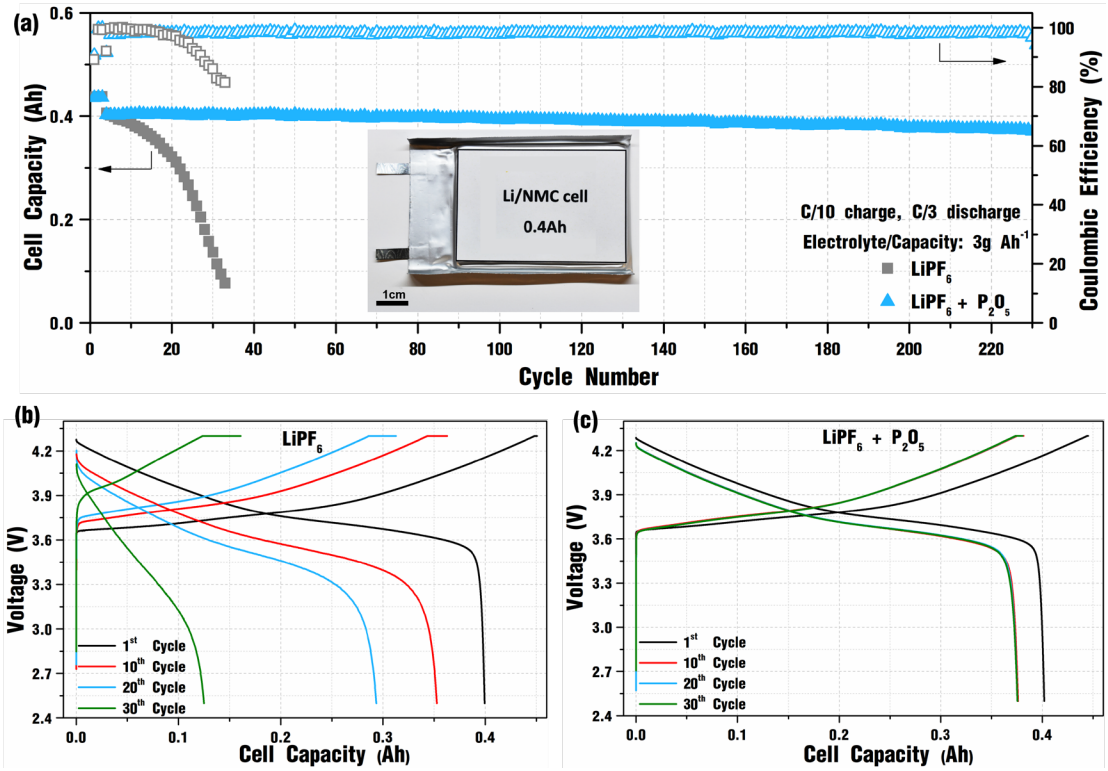

Figure 1. (a) Cycling performance of Li||NMC622 pouch cells with 0.4 Ah capacity (50-µm Li on each side of the anode, 3 mAh cm^{-2} NMC622 on each side of the cathode) in lean electrolyte (electrolyte to capacity ratio of 3 g Ah^{-1}) with the commercial (grey square) or P_2O_5-modified (blue triangle) 1M $LiPF_6$ electrolyte in EC/DEC (50/50 v/v). Inset: photograph of a representative Li||NMC622 pouch cell. Voltage profiles at representative cycles in (b) commercial or (c) P_2O_5-modified electrolyte.

The excellent Li||NMC622 pouch cell performance is clearly rooted from the electrolyte modification by P_2O_5. Liquid-state ^{19}F, ^{31}P, ^{1}H, and ^{13}C nuclear magnetic resonance (NMR) measurements were performed on the commercial and P_2O_5-modified electrolytes to understand how P_2O_5 affects electrolyte reaction products and speciation. Quantitative single-pulse ^{19}F and ^{31}P NMR spectra of the commercial $LiPF_6$ electrolyte (black spectra, **Figure 2**) reveal not only the presence of PF_6^- anions, as expected, but HF and difluorophosphoric acid (HPO_2F_2, species B) as degradation products. Integration of the ^{19}F signal intensities indicate that the molar ratio of HF to PF_6^- is 3.8 x 10^{-3}, yielding an HF concentration of approximately 3.8 mM as the PF_6^- concentration

will only be perturbed from 1 M due to electrolyte reactions. Upon reaction with P_2O_5, the ^{19}F and ^{31}P NMR spectra (red spectra, Figure 2) establish that both HF and HPO_2F_2 have been completely consumed. New species including phosphorous oxyfluoride (POF_3), the oxygen-bridged $OF_2P\text{-}O\text{-}PF_5^-$ anion, and ethyl difluorophosphate ($C_2H_5OPOF_2$) (species C, D, and E, respectively) are formed in the modified electrolyte. Integration of the ^{31}P NMR signals of the P_2O_5-modifed electrolyte indicate that the molar ratios of OPF_3, $C_2H_5OPOF_2$, and $OF_2P\text{-}O\text{-}PF_5^-$ to PF_6^- are approximately 0.01, 0.01 and 0.03, respectively. All ^{19}F and ^{31}P NMR isotropic shifts and *J*-couplings are listed in **Table 1**, whose values are consistent with their signal assignments.

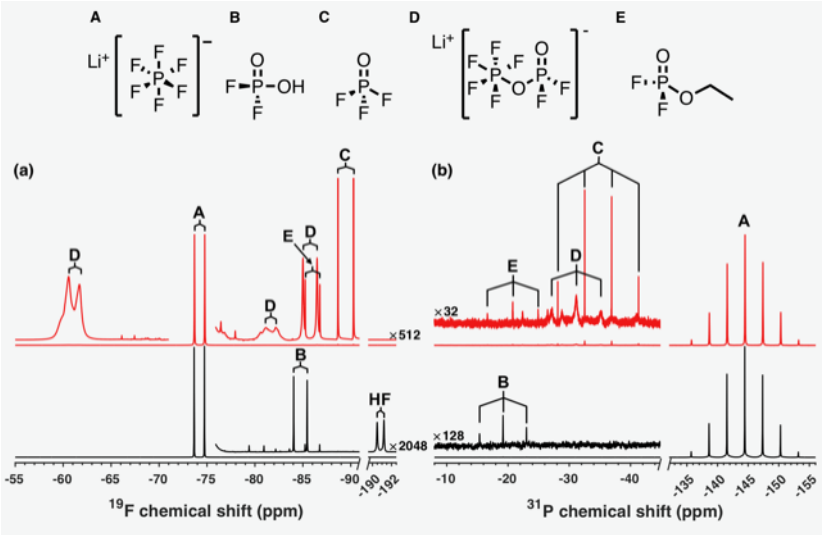

Figure 2. Liquid-state (a) ^{19}F and (b) ^{31}P single-pulse NMR spectra of commercial (black) or P_2O_5-modified (red) 1 M $LiPF_6$ electrolyte in EC/DEC (50/50 v/v). Chemical structures of the major electrolyte species are labelled above the spectra, where their ^{19}F and ^{31}P moieties are indicated in the corresponding NMR spectra.

Table 1. Key electrolyte species and their ^{19}F and ^{31}P NMR isotropic chemical shifts and *J*-couplings.

Species	^{19}F Isotropic Shift (ppm) & Splitting Pattern		^{31}P Isotropic Shift (ppm) & Splitting Pattern		*J*-coupling (Hz)	Label (Fig. 2)
HF	-190.8	doublet	--	--	472 ($^1J_{F\text{-}H}$)	HF
$LiPF_6$	-74.2	doublet	-144.5	septet	709 ($^1J_{F\text{-}P}$)	A
HPO_2F_2	-84.7	doublet	-19.2	triplet	930 ($^1J_{F\text{-}P}$)	B
POF_3	-89.5	doublet	-34.7	quartet	1068 ($^1J_{F\text{-}P}$)	C

$OF^{a}{}_2P^{a}$-O-$P^{b}(F^{b})_4F^{c}$	-85.7[a] -61.1[b] -81.7[c]	doublet doublet doublet	-31.1[a] *ca.*-146[b]	triplet[a] singlet[b]	973[a] 753[b], 750[c] ($^1J_{F-P}$)	D
$C_2H_5OPOF_2$	-86.0	doublet	-20.8	triplet	1006 ($^1J_{F-P}$)	E

Additional NMR experiments aided signal assignments: a single-pulse ^{19}F NMR spectrum of the commercial electrolyte acquired with ^{1}H decoupling (**Figure S3** in the Supporting Information) causes the collapse of the ^{19}F doublet at -190.8 ppm to a singlet, confirming the ^{19}F moiety is covalently bonded to one proton and thus its assignment to HF. A 2D $^{19}F\{^{31}P\}$ through-bond correlation NMR experiment on the P_2O_5-modifed electrolyte (**Figure S4** in the Supporting Information) reveals ^{31}P environments near -146 ppm (otherwise obscured by the intense $LiPF_6$ ^{31}P signal at 144.5 ppm) and at -31.1 ppm, which are covalently bonded to their ^{19}F equatorial $F_4{}^b$ moieties at -61.1 ppm and $F_2{}^a$ moieties at -85.7 ppm (Table 1), respectively, thus confirming the formation of OF_2P-O-PF_5^- anion. Note that the liquid-state ^{31}P NMR measurements also establish that no soluble P_2O_5 species are present within the electrolyte. Interestingly, quantitative single-pulse ^{1}H and ^{13}C NMR spectra of the P_2O_5-modifed electrolyte (**Figure S5** in the Supporting Information) reveal that $C_2H_5OPOF_2$ is produced from the reaction with DEC, while EC is stable.

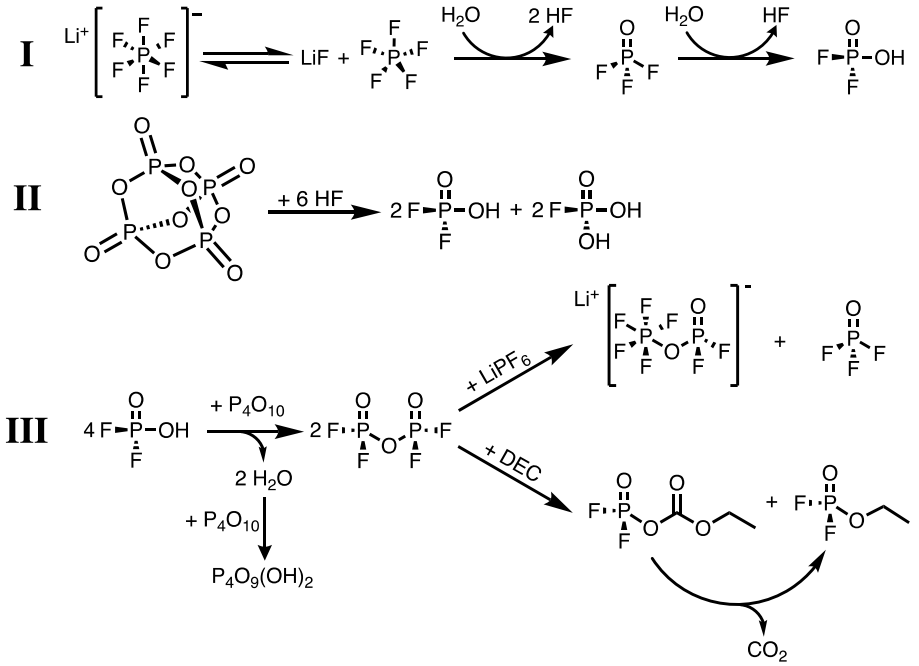

Scheme 1. Electrolyte reaction mechanisms: (I) Decomposition of $LiPF_6$ electrolyte induced by H_2O to produce HF and HPO_2F_2; (II) HF scavenging reaction of P_2O_5; (III) Reactions of products from (II) with P_2O_5 and electrolyte species.

The reaction mechanisms due to electrolyte modification by P_2O_5 are illustrated in **Scheme 1**. $LiPF_6$ degrades to generate HF and HPO_2F_2 in the commercial electrolyte (Reaction I).[37] By introducing P_2O_5, it reacts with HF to generate HPO_2F_2 and monofluorophosphoric acid (H_2PO_3F) (Reaction II). HPO_2F_2 undergoes dehydration induced by P_2O_5 to form the corresponding acid anhydride, while the generated water is absorbed by excess P_2O_5 (Reaction III).[38] Then, the OF_2P-O-$PF5^-$ anion and POF_3 are formed via the reaction between the acid anhydride and PF_6^- anion (top branch, Reaction III), while the acid anhydride also reacts to DEC to form $C_2H_5OPOF_2$. Any oligomerized anhydride of H_2PO_3F,[39] or H_2O-absorbed P_2O_5 were removed by centrifugation during electrolyte preparation. Thus, P_2O_5 scavenges H_2O and HF, while reacting with mono- and di-fluorophosphoric acids, and the carbonate species in the electrolyte to form additional soluble phosphorous-containing compounds that play a

critical role in stabilizing the lithium metal SEI, as shown below.

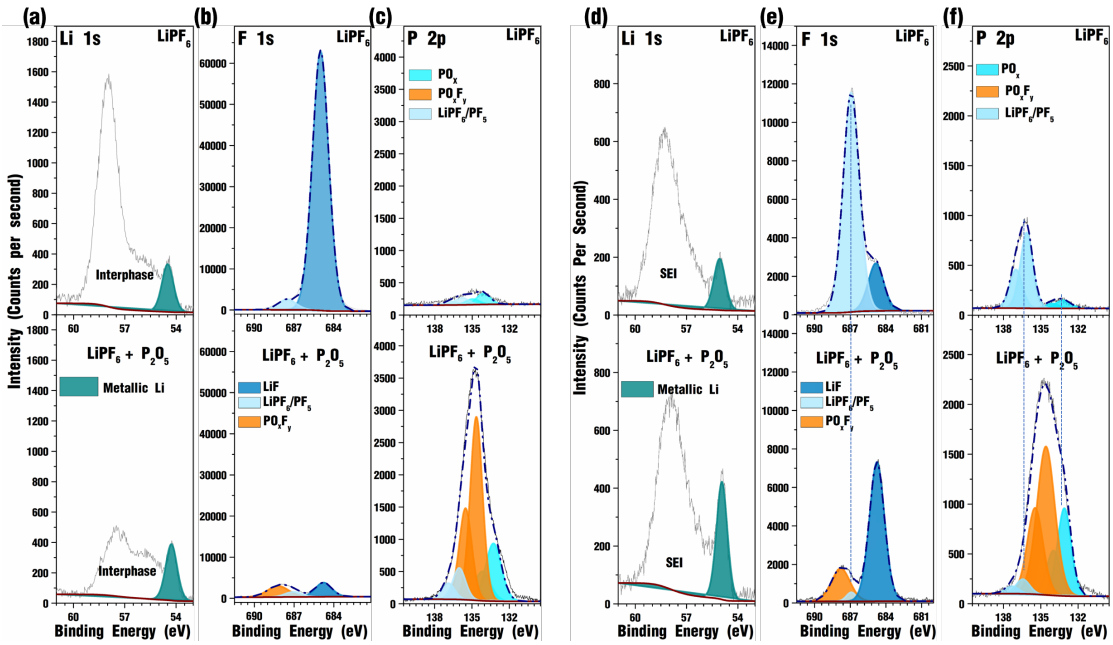

Figure 3. (a) Li 1s, (b) F 1s, and (c) P 2p XPS spectra of the Li metal surface after immersion in the commercial (top) or P_2O_5-modified (bottom) $LiPF_6$ electrolyte for 48 hours. (d) Li 1s, (e) F 1s, and (f) P 2p XPS spectra of the Li surface after a 10-hour galvanostatic deposition (0.3 mA cm^{-2}) in the commercial (top) or P_2O_5-modified (bottom) electrolyte.

The chemical compatibility between the Li anode and the $LiPF_6$ electrolyte is significantly improved by P_2O_5 modification. As displayed in **Figure 3a**, the Li 1s X-ray photoelectron spectroscopy (XPS) spectra detect significant amount of Li-containing passivation layer on the Li surface after immersion in the commercial electrolyte for 48 hours, using the metallic Li peak (54.8 eV) as the reference.[40,41] On the contrary, the Li-containing passivation layer on the Li surface in the P_2O_5-modified $LiPF_6$ electrolyte decreased significantly. The F 1s XPS spectra in **Figure 3b** suggest that a major component of the passivation layer from the commercial electrolyte is LiF,[22,42] while the LiF content on the Li surface from the P_2O_5-modified electrolyte is drastically lower. This observation indicates that the side reaction between HF and Li

metal is significantly alleviated in the P_2O_5-modifed electrolyte. The C 1s and O 1s XPS spectra (**Figure S6** in the Supporting Information) also indicate the existence of Li carbonate (Li_2CO_3) and Li hydroxide in the passivation layer. The P 2p XPS spectra in **Figure 3c** show minimal P-containing species on the Li surface from the commercial electrolyte, which can be assigned to residual $LiPF_6$ and phosphoryl species (PO_x). Interestingly, a P-rich interphase is formed on the Li surface immersed in the electrolyte modified by P_2O_5. The deconvolution of the P 2p XPS spectrum identifies fluorophosphate (PO_xF_y) as the dominant species,[43-45] followed by PO_x. Although the precise speciation of the PO_xF_y-rich interphase needs further determination, clearly the P-rich SEI is formed by reactions between the Li metal anode and the new P-containing species in the P_2O_5-modified electrolyte. Intermittent EIS analysis (**Figure S7** in the Supporting Information) during the chemical stability test reveals continuously increasing interfacial resistance on the Li surface in the commercial electrolyte, while the resistance in the one modified by P_2O_5 remains low and constant.

The SEI formed during the Li deposition was also analyzed via XPS after a 10-hour galvanostatic deposition at 0.3 mA cm^{-2}. The comparison of Li 1s spectra (**Figure 3d**) indicates thicker SEI formation on the Li surface from the commercial electrolyte, using the intensity of Li metal as the reference. The F 1s spectra (**Figure 3e**) identify LiF as a major compound in the SEI formed in the P_2O_5-modified electrolyte, and it is likely derived from the electrochemical reduction of the new species generated in the electrolyte including $C_2H_5OPOF_2$ and $OF_2P\text{-}O\text{-}PF5^-$ anion (Scheme 1). In addition, PO_xF_y and PO_x, which may be either anionic or neutral species, are identified in the SEI

formed in the P_2O_5-modified electrolyte but PO_xF_y absent from the SEI formed in the commercial one. The C 1s and O 1s XPS spectra (**Figure S8** in the Supporting Information) also indicate that the Li_2CO_3 content is reduced in the SEI formed in the P_2O_5-modified electrolyte. Overall, chemical analysis on the chemically formed interphase and the SEI formed during Li deposition unambiguously demonstrate that the critical difference in the P_2O_5-modified electrolyte is the P-rich layer on the Li anode containing the PO_xF_y species, which is the key component for forming a stable SEI. The average CE of Li deposition and stripping in the P_2O_5-modified electrolyte is 97.6%, which is significantly higher than that of 96.0% in the pristine $LiPF_6$ electrolyte (**Figure S9** in the Supporting Information).

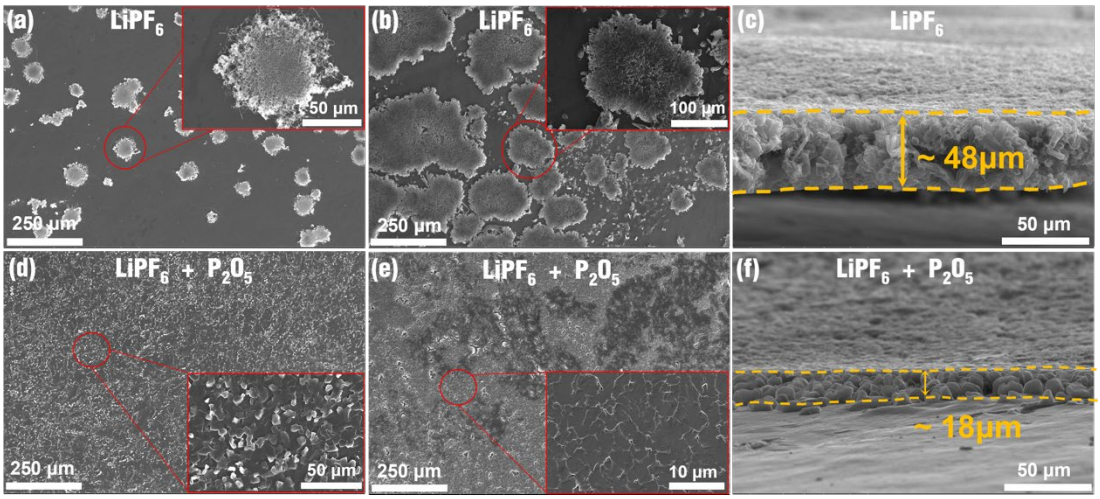

Figure 4. Top view SEM images of Li galvanostatically deposited on Li metal (0.3 mA cm^{-2}) for (a, d) 1 hour and (b, e) 10 hours in the (a, b) commercial and (d, e) P_2O_5-modified $LiPF_6$ electrolyte. Cross-sectional SEM images of Li galvanostatically deposited (0.3 mA cm^{-2}) for 10 hours in the (c) commercial and (f) P_2O_5-modified electrolyte.

The superior Li electrodeposition in the P_2O_5-modified $LiPF_6$ electrolyte is visualized via the SEM measurements. The top-view SEM images of Li deposition on a pure Li metal substrate from the commercial $LiPF_6$ electrolyte after 1 hour and 10

hours at 0.3 mA cm^{-2} are shown in **Figures 4a** and **4b**, respectively. Clearly, Li nucleation and deposition is not uniform due to severe Li surface passivation. Typical whisker-like Li deposits form due to side reactions during electrodeposition (insets).[46-48] After 10-hour of deposition (3 mAh cm^{-2} areal capacity), the thickness of the Li layer is approximately 48 μm (**Figure 4c**), which is much higher than the calculated thickness of 3 mAh cm^{-2} Li deposition, which is 15 μm. In stark contrast, Li nucleation density in the P_2O_5-modified electrolyte is significantly enhanced (**Figure 4d**). The Li deposition after 10-hour deposition (3 mAh cm^{-2} capacity) is uniform and dense (**Figure 4e**), while the thickness of the Li layer is only 18 μm, which is very close to the calculated thickness. SEM characterization thus provides clear evidence that the PO_xF_y-rich SEI plays an essential role in stabilizing Li deposition. The comparison of the Li morphology in the early stage of deposition is shown in **Figure S10** in the Supporting Information.

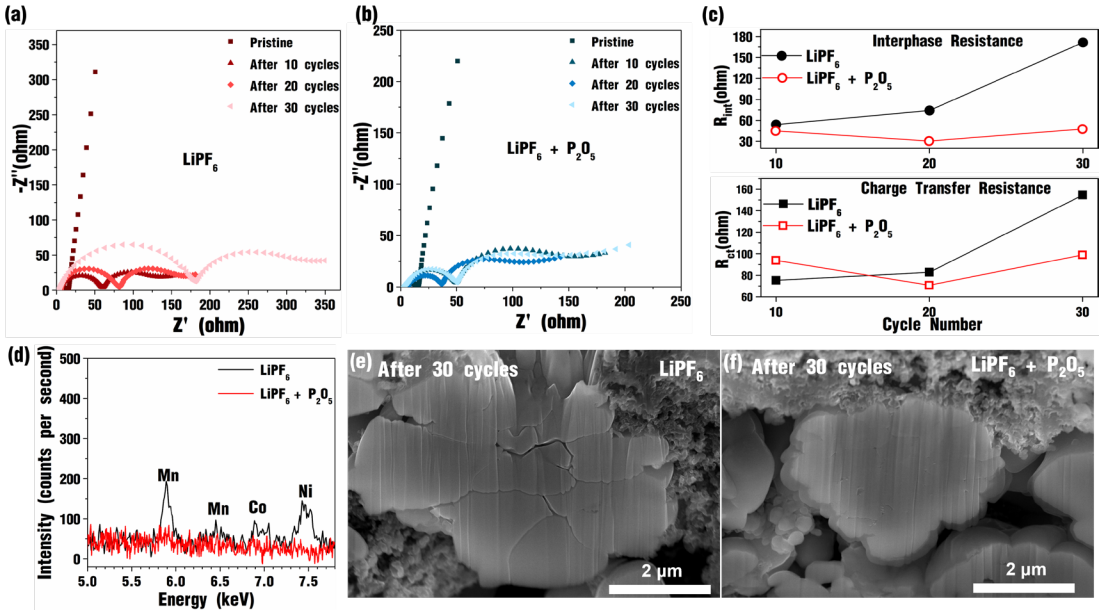

Figure 5. EIS Nyquist plots of the NMC622 cathode acquired after different cycle numbers in Li||NMC622 cells using the (a) commercial or (b) P_2O_5-modified $LiPF_6$ electrolyte. (c) The interfacial and charge transfer resistances of the NMC622 cathode

after every 10th cycle in the P_2O_5-modified electrolyte. (d) EDS spectra of Li metal anode after 30 cycles in the commercial (black) or P_2O_5-modified (red) electrolyte. FIB-SEM images of the NMC622 particles after 30 cycles in the (e) commercial and (f) P_2O_5-modified electrolyte.

The presence of HF in the commercial $LiPF_6$ electrolyte is not only detrimental to the Li anode but also impairs the NMC622 cathode, as shown in **Figure 5**. EIS analyses indicate that both the interfacial and charge transfer resistances of the NMC622 cathode in the Li||NMC622 cells using the commercial electrolyte continuously increase during cycling (**Figure 5a, c**). On the other hand, the interfacial and charge transfer resistances of the NMC622 cathode in the P_2O_5-modified electrolyte remain almost constant during cycling (**Figure 5b**, **c)**. The increasing resistance at the NMC622 cathode contributes to the increasing charge-discharge voltage hysteresis observed during cycling. Furthermore, cathode transition metal (TM) dissolution due to the TM^{2+} (TM = Co, Ni, and Mn) leaching by HF may contribute to the hystersis.[49] Energy- dispersive X-ray spectroscopy (EDS) analysis of the Li anode after 30 cycles in the Li||NMC622 full cells using commercial $LiPF_6$ electrolyte detected significant transition metal content, including Mn, Co and Ni. Clearly, these metals are leaching out of the NMC622 cathode then diffusing and migrating to the anode, which would worsen Li deposition behavior.[50] In contrast, the EDS spectrum of the Li anode after 30 cycles in the P_2O_5-modified $LiPF_6$ electrolyte shows the distinct absence of Mn, Co, and Ni signals. This result proves that eliminating HF from the electrolyte through modification by P_2O_5, as determined via NMR spectroscopy (Figure 2a), eliminates leaching of transition metals. Particle cracking is also a common problem for high-Ni cathode materials due to the precipitation of transition metal fluorides on the exposed cracking surface,[27] leading to

increasing cell impedance and continuous loss of active material. A focused ion beam SEM (FIB-SEM) image of a cross-section of NMC622 particles after 30 cycles in the Li||NMC622 pouch cell reveals that that they are cracked when using the commercial $LiPF_6$ electrolyte (**Figure 5d**), while the NMC622 particles remain crack-free in the P_2O_5-modified $LiPF_6$ electrolyte (**Figure 5e**). Another known problem for NMC cathode materials is releasing highly reactive oxygen (O_2) from the layered oxide lattice at high voltage, and large amount of carbon dioxide (CO_2) can be generated due to the oxidation of carbonate solvents.[51,52] Gas analysis from the pouch cells using the electrolytes with and without P_2O_5 modification is investigated with the differential electrochemical mass spectrometry.[36] The results (**Figure S11** in the Supporting Information) clearly show that CO_2 and O_2 generated during the charging process is greatly reduced in the P_2O_5-modified electrolyte comparing to the commercial one. We believe that the lower charge overpotential and eliminating transition metal dissolution in the P_2O_5-modified electrolyte put much less stress on the cathode lattice, resulting in reduced O_2 release and CO_2 generation.[53]

Conclusion

In summary, we revealed that commercial $LiPF_6$ carbonate electrolytes can be significantly improved for use in Li metal batteries via a simple modification with P_2O_5. The results indicate that adding P_2O_5 removes HF from the electrolyte and generates PO_xF_y species which form a favorable SEI. The new electrolyte is also capable of eliminating transition metal leaching and particle cracking of a NMC622 cathode. Excellent electrochemical performance of Li||NMC622 pouch cells with realistic cell

parameters demonstrate the effectiveness of this simple and scalable approach. The precise speciation of the PO_xF_y-rich SEI and effects of electrolyte aging are underway to gain a better understanding of this promising new electrolyte.

ASSOCIATED CONTENT

Supporting Information

Supporting data and figures including photographs of the pouch cell holder, differential capacity plots, liquid-state ^{19}F NMR in HF region, liquid-state 2D $^{19}F\{^{31}P\}$ HMQC through-bond correlation NMR, liquid-state ^{1}H and ^{13}C single-pulse NMR, C 1s, O 1s, and Li 1s XPS spectra, EIS Nyquist plots of Li passivation tests, CE measurements, SEM images of Li deposition at different durations, and DEMS results.

AUTHOR INFORMATION

Corresponding Authors

Robert J. Messinger - Department of Chemical Engineering, The City College of New York, CUNY, New York, NY 10031, United States; Email: rmessinger@ccny.cuny.edu

Juchen Guo - Materials Science and Engineering Program, Department of Chemical and Environmental Engineering, University of California – Riverside, Riverside, CA 92521, USA; Email: jguo@engr.ucr.edu

Author Contributions

[#]J.Z and J.S. are co-first authors.

Notes

The authors declare no competing financial interest.

ACKNOWLEDGMENT

J.Z., J.S., and J.G. are grateful for the financial support from the University of California, Riverside. The authors acknowledge the use of facilities and instrumentation at the UC Irvine Materials Research Institute (IMRI), which is supported in part by the National Science Foundation through the UC Irvine Materials Research Science and Engineering Center (DMR-2011967). XPS work was performed at the UC Irvine Materials Research Institute (IMRI) using instrumentation funded in part by the National Science Foundation Major Research Instrumentation Program under grant no. CHE-1338173. The authors also would like to thank Dr. Ich Tran (IMRI) for the assistance of samples transfer and quantifying XPS spectra. L.W.G. and R.J.M. acknowledge funding from the U.S. National Science Foundation (NSF) through NSF CAREER award CBET-1847552. All ^{19}F, ^{31}P, ^{1}H, and ^{13}C NMR measurements were acquired at the City University of New York (CUNY) Advanced Science Research Center (ASRC) NMR facility, except 2D $^{19}F\{^{31}P\}$ through-bond correlation experiments, which were acquired at the New York Structural Biology Center (NYSBC). The NYSBC NMR data was made possible by National Institute of Health (NIH) ORIP facility improvement grant CO6RR015495, while the NYSBC 700 MHz spectrometer was purchased with funds from NIH grant S10OD018509. The authors thank Dr. Linxiao Geng at the Oak ridge National Laboratory for the DEMS measurement.

REFERENCES

(1) Pasta, M.; Armstrong, D.; Brown, Z.L.; Bu, J.; Castell, M.R.; Chen, P.; Cocks, A.; Corr, S.A.; Cussen, E.J.; Darnbrough, E.; Deshpande, V.; 2020 Roadmap on Solid-State Bbatteries. *J. Phys.: Energy* **2020**, *2*, 032008.

(2) Xu, L.; Lu, Y.; Zhao, C.Z.; Yuan, H.; Zhu, G.L.; Hou, L.P.; Zhang, Q.; Huang, J.Q. 2021. Toward the Scale-Up of Solid-State Lithium Metal Batteries: The Gaps between Lab-Level Cells and Practical Large-Format Batteries. *Adv. Energy Mater.* **2021**, *11*, 2002360.

(3) Zheng, F.; Kotobuki, M.; Song, S.; Lai, M.O.; Lu, L. Review on Solid Electrolytes for All-Solid-State Lithium-ion Batteries. *J. Power Sources* **2018**, *389*, 198-213.

(4) Chen, S.; Zheng, J.; Mei, D.; Han, K. S.; Engelhard, M. H.; Zhao, W.; Xu, W.; Liu, J.; Zhang, J. G. High-Voltage Lithium-Metal Batteries Enabled by Localized High-Concentration Electrolytes. *Adv. Mater.* **2018**, *30*, 1706102.

(5) Cao, X.; Jia, H.; Xu, W.; Zhang, J. G. Localized High-Concentration Electrolytes for Lithium Batteries. *J. Electrochem. Soc.* **2021**, *168*, 010522.

(6) Lin, S.; Hua, H.; Li, Z.; Zhao, J. Functional Localized High-Concentration Ether-Based Electrolyte for Stabilizing High-Voltage Lithium-Metal Battery. *ACS Appl. Mater. Interfaces* **2020**, *12*, 33710-33718.

(7) Su, C.C.; He, M.; Cai, M.; Shi, J.; Amine, R.; Rago, N.D.; Guo, J.; Rojas, T.; Ngo, A.T.; Amine, K. Solvation-Protection-Enabled High-Voltage Electrolyte for Lithium Metal Batteries. *Nano Energy* **2022**, *92*, 106720.

(8) Su, C.C.; He, M., Shi, J.; Amine, R.; Zhang, J.; Guo, J.; Amine, K. Superior Long-Term Cycling of High-Voltage Lithium-ion Batteries Enabled by Single-Solvent Electrolyte. Nano Energy **2021**, *89*, 106299.

(9) Su, C.C.; He, M.; Amine, R.; Rojas, T.; Cheng, L.; Ngo, A.T.; Amine, K. Solvating Power Series of Electrolyte Solvents for Lithium Batteries. *Energy Environ. Sci*, **2019**, *12*, 1249-1254.

(10) He, M.; Hu, L.; Xue, Z.; Su, C.C.; Redfern, P.; Curtiss, L.A.; Polzin, B.; von Cresce, A.; Xu, K.; Zhang, Z.; Fluorinated Electrolytes for 5-V Li-ion Chemistry: Probing

Voltage Stability of Electrolytes with Electrochemical Floating Test. *J. Electrochem. Soc.* **2015**, 162, A1725.

(11) Beltran, S. P.; Cao, X.; Zhang, J. G.; El-Khoury, P. Z.; Balbuena, P. B. Influence of Diluent Concentration in Localized High Concentration Electrolytes: Elucidation of Hidden Diluent-Li^+ Interactions and Li^+ Transport Mechanism. *J. Mater. Chem. A* **2021**, *9*, 17459-17473.

(12) Ren, F.; Li, Z.; Chen, J.; Huguet, P.; Peng, Z.; Deabate, S. Solvent–Diluent Interaction-Mediated Solvation Structure of Localized High-Concentration Electrolytes. *ACS Appl. Mater. Interfaces* **2022**, DOI:10.1021/acsami.1c21638

(13) Zheng, Y.; Soto, F. A.; Ponce, V.; Seminario, J. M.; Cao, X.; Zhang, J. G.; Balbuena, P. B. Localized High Concentration Electrolyte Behavior Near a Lithium–Metal Anode Surface. *J. Mater. Chem. A* **2019**, *7*, 25047-25055.

(14) He, X.; Bresser, D.; Passerini, S.; Baakes, F.; Krewer, U.; Lopez, J.; Mallia, C.T.; Shao-Horn, Y.; Cekic-Laskovic, I.; Wiemers-Meyer, S.; Soto, F.A. The Passivity of Lithium Electrodes in Liquid Electrolytes for Secondary Batteries. *Nature Rev. Mater.* **2021**, *6*, 1036-1052.

(15) Horstmann, B.; Shi, J.; Amine, R.; Werres, M.; He, X.; Jia, H.; Hausen, F.; Cekic-Laskovic, I.; Wiemers-Meyer, S.; Lopez, J.; Galvez-Aranda, D. Strategies towards Enabling Lithium Metal in Batteries: Interphases and Electrodes. *Energy Environ. Sci.* **2021**, *14*, 5289-5314.

(16) Xia, L.; Jiang, Y.; Pan, Y.; Li, S.; Wang, J.; He, Y.; Xia, Y.; Liu, Z.; Chen, G.Z. Lithium Bis (fluorosulfony) imide-Lithium Hexafluorophosphate Binary-Salt

Electrolytes for Lithium-Ion Batteries: Aluminum Corrosion Behaviors and Electrochemical Properties. *ChemistrySelect*, **2018**, *3*,1954-1960.

(17) Shi, J.; Zhang, J.; Guo, J. Avoiding Pitfalls in Rechargeable Aluminum Batteries Research. *ACS Energy Lett*. **2019**, *4*, 2124-2129.

(18) Aravindan, V.; Gnanaraj, J.; Madhavi, S.; Liu, H. K. Lithium-ion Conducting Electrolyte Salts for Lithium Batteries. *Chem-Eur J* **2011,** *17*, 14326-14346.

(19) Kawamura, T.; Okada, S.; Yamaki, J. Decomposition Reaction of $LiPF_6$-based Electrolytes for Lithium Ion Cells. *J. Power Sources* **2006**, *156*, 547-554.

(20) Lux, S. F.; Chevalier, J.; Lucas, I. T.; Kostecki, R. The Mechanism of HF Formation in $LiPF_6$ based Organic Carbonate Electrolytes. *Electrochem. Commun.* **2012**, *14*, 47-50.

(21) Terborg, L.; Nowak, S.; Passerini, S.; Winter, M.; Karst, U.; Haddad, P. R.; Nesterenko, P. N. Ion Chromatographic Determination of Hydrolysis Products of Hexafluorophosphate Salts in Aqueous Solution. *Anal. Chim. Acta* ,**2012**, *714*, 121-126.

(22) Zhang, J.; Shi, J.; Wen, X.; Zhao, Y.; Guo, J. Properties of Thin Lithium Metal Electrodes in Carbonate Electrolytes with Realistic Parameters. *ACS Appl. Mater. Inter.* **2020**, *12*, 32863-32870.

(23) Parimalam, B. S.; MacIntosh, A. D.; Kadam, R.; Lucht, B. L. Decomposition Reactions of Anode Solid Electrolyte Interphase (SEI) Components with $LiPF_6$. *J. Phys. Chem. C*, **2017**, *121*, 22733-22738.

(24) Agubra, V. A.; Fergus, J. W. The Formation and Stability of the Solid Electrolyte Interface on the Graphite Anode. *J. Power Sources* **2014**, *268*, 153-162.

(25) Vetter, J.; Nováka, P.; Wagner, M. R.; Veit, C.; Möller, K. C.; Besenhard, J. O.; Winter, M.; Wohlfahrt-Mehrens, M.; Vogler, C.; Hammouched, A. Ageing Mechanisms in Lithium-ion Batteries. *J. Power Sources* **2005**, *147*, 269-281.

(26) Zhan, C.; Wu, T. P.; Lu, J.; Amine, K. Dissolution, Migration, and Deposition of Transition Metal Ions in Li-ion Batteries Exemplified by Mn-based Cathodes - A Critical Review. *Energy Environ. Sci.* **2018**, *11*, 243-257.

(27) Schipper, F.; Erickson, E. M.; Erk, C.; Shin, J. Y.; Chesneau, F. F.; Aurbach, D. Recent Advances and Remaining Challenges for Lithium Ion Battery Cathodes I. Nickel-Rich, $LiNi_xCo_yMn_zO_2$. *J. Electrochem. Soc.* **2016**, *164*, A6220.

(28) Han, J. G.; Kim, K.; Lee, Y.; Choi, N. S. Scavenging Materials to Stabilize $LiPF_6$-Containing Carbonate-Based Electrolytes for Li-Ion Batteries. *Adv. Mater.* **2019**, 31, 1804822.

(29) Li, W. T.; Lucht, B. L. Lithium-Ion Batteries: Thermal Reactions of Electrolyte with the Surface of Metal Oxide Cathode Particles. *J. Electrochem. Soc.* **2006**, 153, A1617-A1625.

(30) Xu, C.; Renault, S.; Ebadi, M.; Wang, Z. H.; Bjorklund, E.; Guyomard, D.; Brandell, D.; Edstrom, K.; Gustafsson, T. LiTDI: A Highly Efficient Additive for Electrolyte Stabilization in Lithium-Ion Batteries. *Chem. Mater.* **2017**, 29, 2254-2263.

(31) Sun, X.; Lee, H. S.; Yang, X. Q.; McBreen, J. Using a Boron-based Anion Receptor Additive to Improve the Thermal Stability of $LiPF_6$-based Electrolyte for Lithium Batteries. *Electrochem. Solid St.* **2002**, *5*, A248-A251.

(32) Gordon, I.; Genies, S.; Larbi, G.; Boulineau, A.; Daniel, L.; Alias, M. Original Implementation of Electrochemical Impedance Spectroscopy (EIS) in Symmetric Cells: Evaluation of Post-mortem Protocols Applied to Characterize Electrode Materials for Li-ion Batteries *J. Power Sources* **2016**, 307, 788-795.

(33) Zhang, X.; Ju, Z.; Housel, L. M.; Wang, L.; Zhu, Y.; Singh, G.; Sadique, N.; Takeuchi, K. J.; Takeuchi, E. S.; Marschilok, A. C.; Yu, G. Promoting Transport Kinetics in Li-Ion Battery with Aligned Porous Electrode Architectures. *Nano Lett.* **2019**, 19, 8255-8261.

(34) Aurbach, D.; Gofer, Y.; Langzam, J. The Correlation between Surface-Chemistry, Surface-Morphology, and Cycling Efficiency of Lithium Electrodes in a Few Polar Aprotic Systems. *J Electrochem Soc* **1989,** *136*, 3198-3205.

(35) Fairley, N.; Fernandez, V.; Richard-Plouet, M.; Guillot-Deudon, C.; Walton, J.; Smith, E.; Flahaut, D.; Greiner, M.; Biesinger, M.; Tougaard, S.; Morgan, D.; Baltrusaitis, J. Systematic and Collaborative Approach to Problem Solving Using

X-ray Photoelectron Spectroscopy. *Applied Surface Science Advances*, **2021**, 5, 100112.

(36) Geng, L.; Wood, D. L.; Lewis Sr., S. A.; Connatser, R. M.; Li, M.; Jafta, C. J.; Belharouak, I. High Accuracy In-situ Direct Gas Analysis of Li-ion Batteries. *Journal of Power Sources* **2020**, 466, 228211.

(37) Campion, C. L.; Li, W.; Lucht, B. L. Thermal Decomposition of $LiPF_6$-based Electrolytes for Lithium-ion Batteries. *J. Electrochem. Soc.* **2005**, *152*, A2327.

(38) Robinson, E. A. The Preparation and Raman Spectrum of Diphosphoryl Tetrafluoride: Comparison with the Spectrum of Diphosphoryl Tetrachloride. *Canadian J. Chemistry* **1962**, 40, 1725-1729.

(39) Muenow, D. W.; Uy, O. M.; Margrave, J. L. High Molecular Weight Phosphorus Oxyfluorides. *J. Inorganic and Nuclear Chemistry* **1969**, *31*, 3411-3415.

(40) Kowalczy, S. P.; Ley, L.; Mcfeely, F. R.; Pollak, R. A.; Shirley, D. A. X-Ray Photoemission from Sodium and Lithium. *Phys. Rev. B* **1973**, *8*, 3583-3585.

(41) Wood, K. N.; Teeter, G. XPS on Li-Battery-Related Compounds: Analysis of Inorganic SEI Phases and a Methodology for Charge Correction. *ACS Appl. Energy Mater.* **2018**, *1*, 4493-4504.

(42) Grissa, R.; Fernandez, V.; Fairley, N.; Hamon, J.; Stephant, N.; Rolland, J.; Bouchet, R.; Lecuyer, M.; Deschamps, M.; Guyomard, D.; Moreau, P. XPS and

SEM-EDX Study of Electrolyte Nature Effect on Li Electrode in Lithium Metal Batteries. *ACS Appl. Energ. Mater.* **2018**, 1, 5694-5702.

(43) Hekmatfar, M.; Kazzazi, A.; Eshetu, G. G.; Hasa, I.; Passerini, S. Understanding the Electrode/Electrolyte Interface Layer on the Li-rich Nickel Manganese Cobalt Layered Oxide Cathode by XPS. *ACS Appl. Mater. Inter.* **2019**, *11*, 43166-43179.

(44) Musella, E.; Mullali, A.; Ruf, T.; Huth, P.; Tonelli, D.; Aquilanti, G.; Denecke, R.; Giorgetti, M. Detailing the Self-Discharge of a Cathode Based on a Prussian Blue Analogue. *Energies* **2020**, *13*, 4027.

(45) Su, C.-C.; He, M.; Shi, J.; Amine, R.; Zhang, J.; Amine, K. Solvation Rule for Solid-Electrolyte Interphase Enabler in Lithium-Metal Batteries. *Angew. Chem. Int. Edit.* **2020**, *59*, 18229-18233.

(46) Zhang, X.-Q.; Chen, X.; Cheng, X.-B.; Li, B.-Q.; Shen, X.; Yan, C.; Huang, J.-Q.; Zhang, Q. Highly Stable Lithium Metal Batteries Enabled by Regulating the Solvation of Lithium Ions in Nonaqueous Electrolytes. *Angew. Chem. Int. Edit.* **2018**, *57*, 5301-5305.

(47) Chen, T.; Wu, H.; Wan, J.; Li, M.; Zhang, Y.; Sun, L.; Liu, Y.; Chen, L.; Wen, R.; Wang, C. Synthetic poly-dioxolane as universal solid electrolyte interphase for stable lithium metal anodes. *Journal of Energy Chemistry* **2021**, 62, 172-178.

(48) Dai, H.; Dong, J.; Wu, M.; Hu, Q.; Wang, D.; Zuin, L.; Chen, N., Lai, C.; Zhang, G.; Sun, S. Cobalt-Phthalocyanine-Derived Molecular Isolation Layer for Highly Stable Lithium Anode. *Angew. Chem. Int. Edit.* **2021**, *60*, 19852-19859.

(49) Gilbert, J. A.; Shkrob, I. A.; Abraham, D. P. Transition Metal Dissolution, Ion Migration, Electrocatalytic Reduction and Capacity Loss in Lithium-Ion Full Cells. *J. Electrochem. Soc.* **2017**, *164*, A389-A399.

(50) Betz, J.; Brinkmann, J. J.; Nölle, R.; Lürenbaum,C.; Kolek, M.; Stan, M. C.; Winter, M.; Placke, T. Cross Talk between Transition Metal Cathode and Li Metal Anode: Unraveling Its Influence on the Deposition/Dissolution Behavior and Morphology of Lithium. *Adv. Energy Mater.* **2019**, *9*, 1900574.

(51) Renfrew, S. E.; McCloskey, B. D. Quantification of Surface Oxygen Depletion and Solid Carbonate Evolution on the First Cycle of $LiNi_{0.6}Mn_{0.2}Co_{0.2}O_2$ Electrodes. *ACS Appl. Energy Mater.* **2019**, *2*, 3762-3772.

(52) Jung, R.; Metzger, M.; Maglia, F.; Stinner, C.; Gasteiger, H.A. Oxygen Release and its Effect on the Cycling Stability of $LiNi_xMn_yCo_zO_2$ (NMC) Cathode Materials for Li-ion Batteries. *J. Electrochem. Soc.* **2017**, *164*, A1361.

(53) Liu, J.; Du, Z.; Wang, X.; Tan, S.; Wu, X.; Geng, L.; Song, B.; Chien, P. H.; Everett, S. M.; Hu, E. Anionic Redox Induced Anomalous Structural Transition in Ni-rich Cathodes. *Energy Environ. Sci*, **2021**, *14*, 6441-6454.

TOC GRAPHICS